SIAM J. APPL. MATH.
Vol. 70, No. 5, pp. 1634–1654

MULTISCALE MODELING OF PLANAR AND NANOWIRE FIELD-EFFECT BIOSENSORS*

CLEMENS HEITZINGER†, NORBERT J. MAUSER†, AND CHRISTIAN RINGHOFER‡

Abstract. Field-effect nanobiosensors (or BioFETs, biologically sensitive field-effect transistors) have recently been demonstrated experimentally and have thus gained interest as a technology for direct, label-free, real-time, and highly sensitive detection of biomolecules. The experiments have not been accompanied by a quantitative understanding of the underlying detection mechanism. The modeling of field-effect biosensors poses a multiscale problem due to the different length scales in the sensors: the charge distribution and the electric potential of the biofunctionalized surface layer changes on the Ångström length scale, whereas the exposed sensor area is measured in micrometers squared. Here a multiscale model for the electrostatics of planar and nanowire field-effect sensors is developed by homogenization of the Poisson equation in the biofunctionalized boundary layer. The resulting interface conditions depend on the surface charge density and dipole moment density of the boundary layer. The multiscale model can be coupled to any charge transport model and hence makes the self-consistent quantitative investigation of the physics of field-effect sensors possible. Numerical verifications of the multiscale model are given. Furthermore a silicon nanowire biosensor is simulated to elucidate the influence of the surface charge density and the dipole moment density on the conductance of the semiconductor transducer. The numerical evidence shows that the conductance varies exponentially as a function of both charge and dipole moment. Therefore the dipole moment of the surface layer must be included in biosensor models. The conductance variations observed in experiments can be explained by the field effect, and they can be caused by a change in dipole moment alone.

Key words. Poisson equation, multiscale problem, interface conditions, homogenization, numerical simulation, field-effect biosensor, BioFET, nanowire

AMS subject classifications. 35B27, 35J05, 92C05, 92C50

DOI. 10.1137/080725027

1. Introduction.

This work provides the foundation for physics-based modeling of field-effect biosensors. BioFETs (biologically sensitive field-effect transistors) are field-effect biosensors with semiconductor transducers. Their structure is similar to that of MOSFETs (metal-oxide-semiconductor field-effect transistors), but the gate structure is replaced by a biofunctionalized surface layer in an aqueous solution and an electrode (see Figure 1 for the structure of a nanowire BioFET). BioFETs are an emerging nanotechnology with the potential to revolutionize biosensing due to their label-free operation [4, 10, 15, 16].

A cut through a nanowire BioFET is shown in Figure 1. It consists of a semiconductor transducer, usually a silicon nanowire, that is surrounded by a thin dielectric layer, usually silicon oxide. Probe molecules (or receptors) are attached to the transducer in the biofunctionalized boundary layer. The nanowire is surrounded by an

*Received by the editors May 18, 2008; accepted for publication (in revised form) November 3, 2009; published electronically January 13, 2010. This work was supported by the Stadt Wien – ÖAW (Austrian Academy of Sciences) project Multi-scale Modeling and Simulation of Field-Effect Nanobiosensors, by the FWF (Austrian Science Fund) project P20871-N13, by the Austrian Ministry of Science via its grant for the Wolfgang Pauli Institute, and by the EU project DEASE (contract MEST-CT-2005-021122). This work was supported by National Science Foundation award DMS-0718308.

http://www.siam.org/journals/siap/70-5/72502.html

†Faculty of Mathematics and Wolfgang Pauli Institute, University of Vienna, Nordbergstraße 15, A–1090 Vienna, Austria (clemens.heitzinger@univie.ac.at, norbert.mauser@univie.ac.at).

‡Department of Mathematics, Arizona State University, Tempe, AZ 85287 (ringhofer@asu.edu).

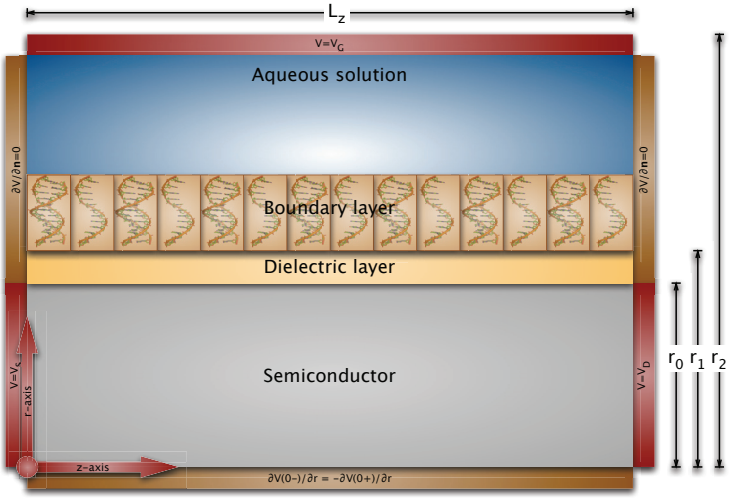

FIG. 1. *Schematic diagram of a nanowire BioFET. The r- and z-axes of a cylindrical coordinate system are shown.*

aqueous solution that contains possibly many different types of biomolecules, but only the target molecules can bind to the probe molecules at the surface and are thus detected. In a DNA sensor, shown here, the immobilized probe molecules are ssDNA (single-stranded deoxyribonucleic acid) oligonucleotides and the target molecules are the complementary strands. After hybridization of the two strands in the boundary layer to form dsDNA (double-stranded DNA), the charge distribution in the biofunctionalized boundary layer is changed, and this modulates the conductance of the semiconductor transducer. The conductance is measured between the two contacts on the left and on the right.

The sensor is selective, since only target molecules can bind to the probe molecules, and unspecific binding at the surface is avoided. The sensitivity of the sensor is determined by its electrostatics. Since the electrostatic field in the boundary layer and in the semiconductor is affected by the target molecules, this type of sensor is called a field-effect sensor.

The main advantage of BioFETs is label-free operation, whereas currently available technology works by first labeling the analyte, i.e., the molecules to be detected, with, e.g., fluorescent or radioactive markers and then applying appropriate detection techniques. Label-free devices simplify analyte preparation and thus have technical and economic advantages. Due to label-free operation, further advantages are (near) real-time operation and high sensitivity.

BioFETs have been reproduced by different groups, and there are now good experimental indications that the sensing mechanism is indeed a field effect [4]; i.e., as target molecules bind to the immobilized probe molecules in the surface layer, the charge distribution changes and modulates the conductance of the semiconductor transducer, similarly to the effect that a change in gate voltage has on a MOSFET.

Although consensus has been reached among experimentalists that a field effect is measured, the functioning of BioFETs has not been understood quantitatively [8, 12, 13, 14]. The modeling and simulation of BioFETs is complicated by several facts. First, two systems must be coupled, namely, a biological system, i.e., the biofunctionalized surface layer with the biomolecules in the aqueous solution con-

taining ions, and an electronic system, i.e., the semiconductor transducer. The electrostatics of the biosensors must be calculated self-consistently, and especially the electrostatics of the biofunctionalized surface must be taken into account.

Second, the modeling of BioFETs poses a multiscale problem. The diameters of the biomolecules are in the nanometer range and the spacing between DNA strands on a functionalized silicon-oxide surface has been measured to be between ca. 3 nm and ca. 10 nm [11]. Therefore the charge distribution and the electric potential in the vicinity of the biomolecules varies on the Ångström or nanometer length scale. On the other hand, the length of the transducers, i.e., the distance between the two contacts of the sensors, cannot be smaller than a few dozen nanometers because of technical reasons, and in experiments it is much larger, measuring hundreds of nanometers or a few micrometers. Hence at least four orders of magnitude of difference in length scale must be covered in simulations, and therefore existing device simulators with very large grids that resolve the fine structure of the biomolecules cannot be used due to their computational cost.

This work establishes the basis for the simulation of nanowire and nanoplate BioFETs. The technique for solving the multiscale problem used here is the derivation of interface conditions for the Poisson equation that include the effects of the quasi-periodic biofunctionalized boundary layer. This work also improves previous work where no multiscale models for the biofunctionalized layer were used [3, 5, 6, 7]. In addition the conductance of nanowires is calculated in this work.

The basic model equation is the mean-field Poisson equation in cylindrical coordinates

$$-\nabla \cdot \big(\epsilon(r,\phi,z)\nabla\big)V(r,\phi,z) = n(r,\phi,z)$$

as the continuum model for the electric potential. The biofunctionalized boundary layer at the exterior of the cylinder is split into periodically repeated cells (see Figure 1), and the charge density in the cells of the boundary layer is written as a function of slow and fast variables. The fast variables allow us to zoom in to the boundary layer. The homogenization of the boundary layer starts by passing to the limit where the cell size becomes zero in the weak form of the Poisson equation. This yields the weak formulation of the homogenized problem. Then the problem is reformulated in a strong sense; i.e., a pointwise solution that satisfies certain interface conditions is sought. By converting the ansatz for the strong solution to a weak formulation and then comparing it to the weak formulation of the homogenized problem, the interface conditions are found.

First and second order terms are included in the limit of the cell size approaching zero. The physical interpretation of the second order term is that the resulting interface conditions depend not only on the surface charge density of the boundary layer, but also on its dipole moment density. Therefore the analysis of the boundary layer provides the means to include reconfigurations of the charges in the boundary layer upon binding of target molecules in the model. These reconfigurations of the boundary layer will be investigated in future work. The feasibility to include higher order effects motivates the numerical simulations in section 3 where the conductance of nanowires is calculated as a function of surface charge density and dipole moment density using the drift-diffusion charge transport model.

In this work only the boundary layer in the liquid is homogenized; the inhomogeneous problem on the semiconductor side is the subject of future work and will improve the model for semiconductors in accumulation or inversion mode. The advantage of this work is its generality: it can be implemented in a straightforward manner as an

extension to existing semiconductor simulators, since it can be applied to all types of charge transport models. It should also be noted that in general counter-ions form a layer around biomolecules and especially highly charged molecules like DNA. This screening effect should be included in simulations of field-effect biosensors [2], but the details are not discussed here.

This paper is organized as follows: In section 2.1 we define the basic structure and formulate the model equations; in section 2.2 we formulate the problem as a boundary homogenization problem; and in section 2.3 we solve the homogenization problem. The results are interface conditions which incorporate the microscopic structure of the biofunctionalized surface layer as interface conditions on the macroscopic scale. The corollary for planar geometries is given in section 2.4. Section 3 is devoted to simulation results. First, in sections 3.1 and 3.2, the use of the homogenized problem as a substitute of the original problem is validated numerically in one and two dimensions. Then, in section 3.3, the homogenized problem is used to calculate the conductance of a silicon nanowire biosensor, and the effect of the biofunctionalized surface layer on the conductance is investigated. Finally we conclude in section 4.

2. Homogenization.

2.1. The model equations. We first introduce the coordinate system for the simulation domain (see Figure 1). The origin is on the source contact and on the axis of the cylindrical nanowire; the z-axis points along the axis of the nanowire; r and ϕ are the radius and the angle of the cylindrical coordinate system (r, ϕ, z). The length of the nanowire, i.e., the distance between the source and drain contacts, is L_z. The semiconducting core of the nanowire is at $0 \le r < r_0$, the insulating layer surrounding the nanowire is at $r_0 \le r < r_1$, the aqueous solution is at $r_1 \le r < r_2$, and in the aqueous solution there is an electrode at $r = r_2$. The basic model equation for the electric potential considered in this paper is the mean-field Poisson equation

$$-\nabla \cdot \big(\epsilon(\mathbf{x})\nabla\big)V(\mathbf{x}) = n(\mathbf{x}), \tag{1}$$

where $\mathbf{x} \in \mathbb{R}^3$, V is the electric potential, ϵ is the permittivity, and n is the charge distribution. In cylindrical coordinates it reads

$$\begin{aligned} -\nabla \cdot \big(\epsilon(r,\phi,z)\nabla\big)V(r,\phi,z) \\ = -\left(\frac{1}{r}\partial_r(\epsilon r \partial_r) + \frac{\epsilon}{r^2}\partial_{\phi\phi} + \frac{\epsilon_\phi}{r^2}\partial_\phi + \partial_z(\epsilon\partial_z)\right)V(r,\phi,z) = n(r,\phi,z), \end{aligned} \tag{2}$$

where $r \in [0, r_2]$, $\phi \in [0, 2\pi)$, and $z \in [0, L_z]$. Here n denotes the charge density in the semiconductor and in the dielectric layer (for $r < r_1$) and in the liquid (for $r > r_1$). The Poisson equation (2) ensures self-consistency when charge transport in the semiconducting transducer is calculated using a transport model such as the drift-diffusion model [9] as described in section 3.3.

In the situation of Figure 1, the permittivity ϵ is the piecewise constant function

$$\epsilon(r) := \begin{cases} \epsilon_< \in \mathbb{R} & \text{for } r < r_1, \\ \epsilon_> \in \mathbb{R} & \text{for } r > r_1. \end{cases}$$

Hence we have two conditions at the interface $r = r_1$, namely, the continuity of the potential and the continuity of the electric displacement,

$$V(r_1-, \phi, z) = V(r_1+, \phi, z), \tag{3a}$$

$$\epsilon_< \partial_r V(r_1-, \phi, z) = \epsilon_> \partial_r V(r_1+, \phi, z). \tag{3b}$$

In the semiconductor ($r < r_1$), the charge distribution n in (2) is given by the background density of impurity ions, i.e., the doping of the semiconductor. In the liquid ($r > r_1$), the charge distribution is given by the charges of the biomolecules in the surface layer. Thus we have

$$n(r,\phi,z) := \begin{cases} n_<(r,\phi,z) & \text{for } r < r_1, \\ \chi(r,\phi,z) & \text{for } r > r_1, \end{cases}$$

with $n_<$ being the doping concentration of the semiconductor and χ being the charge density of the surface or boundary layer.

The problem considered here is a homogenization problem, since the surface layer, i.e., the charge density χ, will exhibit a spatial structure which cannot be resolved with a transport model. The main goal of this paper is therefore to replace the problem (2) by a homogenized problem that is subject to interface conditions describing the integral effect of the surface layer charges.

2.2. The fine structure of the biofunctionalized surface layer. We define $\mathbf{y} := (\phi, z) \in [0, 2\pi) \times [0, L_z] =: L$ and divide the interface at $r = r_1$ into $N_1 \times N_2$ periodically repeated cells by defining

$$\mathbf{m} := \begin{pmatrix} 2\pi m_1 \\ L_z m_2 \end{pmatrix} \quad \text{for } m_1, m_2 \in \mathbb{Z}$$

and

$$\mathcal{C}_{\mathbf{m}} := \big[2\pi(m_1 - 1)\lambda, 2\pi m_1 \lambda\big) \times \big[L_z(m_2 - 1)\lambda, L_z m_2 \lambda\big) \quad \text{for } m_1, m_2 \in \mathbb{Z}.$$

The cells $\mathcal{C}_{\mathbf{m}}$ are of size $2\pi\lambda \times L_z\lambda$ so that they cover the whole interface,

$$[0, 2\pi) \times [0, L_z) \subset \bigcup_{\substack{1 \le m_1 \le N_1 \\ 1 \le m_2 \le N_2}} \mathcal{C}_{\mathbf{m}},$$

with $N_1 := \lceil 1/\lambda \rceil$ and $N_2 := \lceil 1/\lambda \rceil$. Each three-dimensional cell $[r_1, r_2] \times \mathcal{C}_{\mathbf{m}}$ contains one probe molecule and possibly one target molecule as depicted in Figure 1. $\lambda \in \mathbb{R}$ denotes the ratio of the spatial scale of the biomolecules to the spatial scale of the sensor and the semiconductor transport picture. Since the biomolecules are several orders of magnitude smaller than the sensors, we have $\lambda \ll 1$. At the interface the Poisson equation (2) shows boundary layer behavior that can be scaled by introducing local coordinates. We stretch the r- and $\mathbf{y}$-coordinates at the interface by a factor of $1/\lambda$ and hence define the fast variables $\rho := r_1 + (r - r_1)/\lambda$ and $\boldsymbol{\eta} := \frac{1}{\lambda}\mathbf{y}$ in contrast to the slow, original variables r and $\mathbf{y}$. Now we make a multiscale ansatz as follows: we write the charge density in the liquid ($r > r_1$) as

$$\chi(r,\phi,z) = \widehat{\chi}\left(r_1 + \frac{r - r_1}{\lambda}, \frac{1}{\lambda}\mathbf{y}, \mathbf{y}\right).$$

For simplicity we denote $\widehat{\chi}$ by χ as well. The function $\chi(\rho, \boldsymbol{\eta}, \mathbf{y})$ is periodic in $\boldsymbol{\eta}$, i.e.,

$$\chi(\rho, \boldsymbol{\eta} + \mathbf{m}, \mathbf{y}) = \chi(\rho, \boldsymbol{\eta}, \mathbf{y}) \qquad \forall m_1 \in \{0, \dots, N_1 - 1\}, \quad \forall m_2 \in \{0, \dots, N_2 - 1\}$$

holds. $\chi(\rho, \boldsymbol{\eta}, \mathbf{y})$ decays to zero for $\rho \to \infty$; i.e., the charges are concentrated close to the surface layer in the liquid.

In addition, the large-scale variation in the immobilized surface layer is given by the additional dependence of $\chi(\rho, \boldsymbol{\eta}, \mathbf{y})$ on the third variable $\mathbf{y}$. Two types of occupation are possible for each cell: a probe molecule having charge density $\chi_1(\rho, \boldsymbol{\eta})$ or a probe molecule bound to a target molecule represented by the charge density $\chi_2(\rho, \boldsymbol{\eta})$. These charge densities are periodically repeated in the $\mathbf{y}$-directions (see Figure 1). The whole charge density can then be written as

$$\chi(\rho, \boldsymbol{\eta}, \mathbf{y}) = K_1(\mathbf{y})\chi_1(\rho, \boldsymbol{\eta}) + K_2(\mathbf{y})\chi_2(\rho, \boldsymbol{\eta}),$$

where $K_1(\mathbf{y})$ and $K_2(\mathbf{y})$ are the probabilities that the surface receptor is in the unbound or bound state. The probabilities $K_1(\mathbf{y})$ and $K_2(\mathbf{y})$ vary slowly along the sensor surface, since the binding efficiency of probe and target molecules might be influenced by, e.g., electrostatic effects at the contacts, but these variations in the free energy would not be localized. This means that $\chi(\rho, \boldsymbol{\eta}, \mathbf{y})$ is a slowly varying function of $\mathbf{y}$ and thus quasi-periodic in $\boldsymbol{\eta}$, since it is a slowly varying linear combination of the two periodic charge distributions $\chi_1(\rho, \boldsymbol{\eta})$ and $\chi_2(\rho, \boldsymbol{\eta})$.

These considerations motivate the following definition.

DEFINITION 1 (boundary layer function). *Let $\Omega := [r_1, r_2] \times [\phi_1, \phi_2] \times [z_1, z_2] \subset \mathbb{R}^3$. A function $\chi \in L^2(\Omega)$ is called a boundary layer function if it can be written in the form*

$$\chi(r, \mathbf{y}) =: \widehat{\chi}\Big(r_1 + \frac{r - r_1}{\lambda}, \frac{1}{\lambda}\mathbf{y}, \mathbf{y}\Big)$$

and if $\widehat{\chi}$ is periodic in its second argument with period Ω. Furthermore

$$\lim_{r\to\infty} \chi(r, \mathbf{y}) = 0 \qquad \forall \lambda \in \mathbb{R}^+$$

and there exists a $\bar{\bar{\chi}} \in \mathbb{R}^+$ so that

$$\|\bar{\chi}\|_2 \le \frac{\bar{\bar{\chi}}}{\lambda^2} \qquad \forall \lambda \in \mathbb{R}^+$$

holds, where

$$\bar{\chi}(r, \mathbf{y}) := \sup_{\mathbf{x}\in\Omega} \Big|\widehat{\chi}\Big(r_1 + \frac{r - r_1}{\lambda}, \frac{1}{\lambda}\mathbf{x}, \mathbf{y}\Big)\Big|.$$

The last assumption means that the growth of the charge density in the cells of the boundary layer is not faster than $1/\lambda^2$. Since the number of cells in the boundary layer increases as λ^2, this assumption is natural and implies that the total charge in the boundary layer remains finite as $\lambda \to 0$.

As will be seen in the next section, the biomolecules will only have an impact on the transport model if their integral charge density is of order $O(1)$, despite the fact that the charges are concentrated close to the surface. This means that $\chi(\rho, \boldsymbol{\eta}, \mathbf{y}) = O(1/\lambda)$ has to hold in order for the problem to be nontrivial. Using the relationship

$$\mathbf{y} = \lambda\mathbf{m} + \lambda\boldsymbol{\eta}$$

so that $\boldsymbol{\eta} \in L$, the charge in cell $\mathcal{C}_{\mathbf{m}}$ can be written as

$$\begin{aligned}\int_{\mathcal{C}_{\mathbf{m}}} \int_{r_1}^{r_2} \chi\left(r_1 + \frac{r-r_1}{\lambda}, \frac{1}{\lambda}\mathbf{y}, \mathbf{y}\right) r \mathrm{d}r\mathrm{d}\mathbf{y} \\ = \lambda^3 \int_L \int_{r_1}^{r_2} \chi\big(\rho, \mathbf{m}+\boldsymbol{\eta}, \lambda(\mathbf{m}+\boldsymbol{\eta})\big)\big(r_1 + \lambda(\rho - r_1)\big)\mathrm{d}\rho\mathrm{d}\boldsymbol{\eta} \\ \approx \lambda^3 \int_L \int_{r_1}^{r_2} \chi(\rho, \boldsymbol{\eta}, \lambda\mathbf{m})\big(r_1 + \lambda(\rho - r_1)\big)\mathrm{d}\rho\mathrm{d}\boldsymbol{\eta},\end{aligned}$$

and hence the total charge of all cells is

$$\begin{aligned}(4) \quad &\approx \sum_{\substack{1\le m_1\le N_1 \\ 1\le m_2\le N_2}} \lambda^3 \int_L \int_{r_1}^{r_2} \chi(\rho, \boldsymbol{\eta}, \lambda\mathbf{m})\big(r_1 + \lambda(\rho - r_1)\big)\mathrm{d}\rho\mathrm{d}\boldsymbol{\eta} \\ &\approx \frac{\lambda}{2\pi r_1 L_z} \int_L \int_L \int_{r_1}^{r_2} \chi(\rho, \boldsymbol{\eta}, \mathbf{y})\big(r_1 + \lambda(\rho - r_1)\big)\mathrm{d}\rho\mathrm{d}\boldsymbol{\eta} r_1 \mathrm{d}\mathbf{y}.\end{aligned}$$

This leads to the following definition.

DEFINITION 2 (macroscopic surface charge density). *Let χ be a boundary layer function. Then the macroscopic surface charge density $C(\mathbf{y})$ is defined as*

$$(5) \qquad C(\mathbf{y}) := \lim_{\lambda\to 0} \frac{\lambda}{2\pi r_1 L_z} \int_L \int_{r_1}^{r_2} \chi(\rho, \boldsymbol{\eta}, \mathbf{y})\big(r_1 + \lambda(\rho - r_1)\big)\mathrm{d}\rho\mathrm{d}\boldsymbol{\eta}.$$

This yields $\int_L C(\mathbf{y}) r_1 \mathrm{d}\mathbf{y}$ as the total charge. We will also consider the case of essentially neutral biomolecules, which, however, carry internal partial charges summing up to zero. In this case we will have to consider dipole distributions in the limit $\lambda \to 0$. Analogously to above (and using the trivial isomorphism $\big(r, (y_1, y_2)\big) \mapsto (r, y_1, y_2)$ to simplify notation), the dipole moment in cell $\mathcal{C}_{\mathbf{m}}$ is given by

$$\begin{aligned}\int_{\mathcal{C}_{\mathbf{m}}} \int_{r_1}^{r_2} \begin{pmatrix} r - r_1 \\ \mathbf{y} - \lambda\mathbf{m}\end{pmatrix} \chi\left(r_1 + \frac{r-r_1}{\lambda}, \frac{1}{\lambda}\mathbf{y}, \mathbf{y}\right) r \mathrm{d}r\mathrm{d}\mathbf{y} \\ \approx \lambda^4 \int_L \int_{r_1}^{r_2} \begin{pmatrix} \rho - r_1 \\ \boldsymbol{\eta}\end{pmatrix} \chi(\rho, \boldsymbol{\eta}, \lambda\mathbf{m})\big(r_1 + \lambda(\rho - r_1)\big)\mathrm{d}\rho\mathrm{d}\boldsymbol{\eta},\end{aligned}$$

and hence the total dipole moment of all cells is

$$\begin{aligned}&\approx \sum_{\substack{1\le m_1\le N_1 \\ 1\le m_2\le N_2}} \lambda^4 \int_L \int_{r_1}^{r_2} \begin{pmatrix} \rho - r_1 \\ \boldsymbol{\eta}\end{pmatrix} \chi(\rho, \boldsymbol{\eta}, \lambda\mathbf{m})\big(r_1 + \lambda(\rho - r_1)\big)\mathrm{d}\rho\mathrm{d}\boldsymbol{\eta} \\ &\approx \frac{\lambda^2}{2\pi r_1 L_z} \int_L \int_L \int_{r_1}^{r_2} \begin{pmatrix} \rho - r_1 \\ \boldsymbol{\eta}\end{pmatrix} \chi(\rho, \boldsymbol{\eta}, \mathbf{y})\big(r_1 + \lambda(\rho - r_1)\big)\mathrm{d}\rho\mathrm{d}\boldsymbol{\eta} r_1 \mathrm{d}\mathbf{y}.\end{aligned}$$

Accordingly this leads to the following definition.

DEFINITION 3 (macroscopic dipole moment density). *Let χ be a boundary layer function. The macroscopic dipole moment density $D(\mathbf{y})$ is defined as*

(6)

$$D(\mathbf{y}) := \begin{pmatrix} D_r(\mathbf{y}) \\ D_{\mathbf{y}}(\mathbf{y})\end{pmatrix} := \lim_{\lambda\to 0} \frac{\lambda^2}{2\pi r_1 L_z} \int_L \int_{r_1}^{r_2} \begin{pmatrix} \rho - r_1 \\ \boldsymbol{\eta}\end{pmatrix} \chi(\rho, \boldsymbol{\eta}, \mathbf{y})\big(r_1 + \lambda(\rho - r_1)\big)\mathrm{d}\rho\mathrm{d}\boldsymbol{\eta}.$$

Note that D_r is a scalar and $D_{\mathbf{y}}$ is a 2-vector. $D(\mathbf{y})$ has a factor λ^2, while $C(\mathbf{y})$ has a factor λ. Therefore the dipole moments are a higher order effect, except in the case when $C = 0$.

2.3. The theorem for the limiting problem. After the discussion of the physical situation and the motivation of the assumptions, we now derive the limiting problem for $\lambda \to 0$ in the fine structure of the biomolecules. The main result is this theorem.

THEOREM 4. *Let* $R := [0, r_2]$, $L := [0, 2\pi) \times [0, L_z]$, *and* $\Omega := R \times L \subset \mathbb{R}^3$. *Let* $r_1 \in (0, r_2)$, *let* $\epsilon : R \to \mathbb{R}^+$ *with*

$$\epsilon(r) = \begin{cases} \epsilon_< \in \mathbb{R}^+ & \text{for } r < r_1, \\ \epsilon_> \in \mathbb{R}^+ & \text{for } r > r_1, \end{cases}$$

and let $n \in L^2(\Omega)$ *with*

$$n(r, \mathbf{y}) := \begin{cases} n_<(r, \mathbf{y}) \in L^2\big([0, r_1) \times L\big) & \text{for } r < r_1, \\ \chi(r, \mathbf{y}) \in L^2\big((r_1, r_2) \times L\big) & \text{for } r > r_1, \end{cases}$$

where $n_<$ *is bounded and* χ *is a boundary layer function such that* $C(\mathbf{y})$ *and* $D_r(\mathbf{y})$ *exist.*

The limiting problem for $\lambda \to 0$ *of the boundary value problem*

$$-\nabla \cdot \big(\epsilon(r)\nabla\big) V(r, \mathbf{y}) = n(r, \mathbf{y}), \tag{7a}$$

$$V(r_1-, \mathbf{y}) = V(r_1+, \mathbf{y}), \tag{7b}$$

$$\epsilon_< \partial_r V(r_1-, \mathbf{y}) = \epsilon_> \partial_r V(r_1+, \mathbf{y}) \tag{7c}$$

with $(r, \mathbf{y}) \in \Omega$ *is the boundary value problem*

$$-\epsilon_< \left(\frac{1}{r} \partial_r (r \partial_r) + \frac{1}{r^2} \partial_{\phi\phi} + \partial_{zz} \right) V_h(r, \mathbf{y}) = n_<(r, \mathbf{y}) \quad \text{for } r < r_1, \tag{8a}$$

$$-\epsilon_> \left(\frac{1}{r} \partial_r (r \partial_r) + \frac{1}{r^2} \partial_{\phi\phi} + \partial_{zz} \right) V_h(r, \mathbf{y}) = 0 \qquad \text{for } r > r_1 \tag{8b}$$

with the interface conditions

$$V_h(r_1+, \mathbf{y}) - V_h(r_1-, \mathbf{y}) = \frac{D_r(\mathbf{y})}{\epsilon_>}, \tag{9a}$$

$$\epsilon_> \partial_r V_h(r_1+, \mathbf{y}) - \epsilon_< \partial_r V_h(r_1-, \mathbf{y}) = -C(\mathbf{y}). \tag{9b}$$

Proof. The weak formulation. To simplify notation, we write χ for $\widehat{\chi}$ as well. We first remove the jump (7c) in the electric field by stretching the r-coordinate for $r < r_1$. To that end, we define the variable transformation

$$W(s(r), \mathbf{y}) := V(r, \mathbf{y}), \tag{10}$$

so that W and $\partial_s W$ become continuous. Since $\epsilon_< \partial_r V(r_1-, \mathbf{y}) = \epsilon_> \partial_r V(r_1+, \mathbf{y})$ is then equivalent to $\epsilon_< s'(r_1-) = \epsilon_> s'(r_1+)$, we define

$$\mu := \frac{\epsilon_>}{\epsilon_<} \qquad \text{and} \qquad s(r) := \begin{cases} \mu(r - r_1) + r_1 & \text{for } r < r_1, \\ r & \text{for } r > r_1 \end{cases} \tag{11}$$

and have $s(r_1) = r_1$ and $r(s) = r_1 + (s - r_1)/\mu$. This gives the Poisson equation

$$-\epsilon_< \left(\frac{\mu^2}{r(s)} \partial_s (r(s) \partial_s) + \frac{1}{r(s)^2} \partial_{\phi\phi} + \partial_{zz} \right) W = n(r(s), \mathbf{y}) \quad \text{for } s < r_1, \tag{12a}$$

$$-\epsilon_> \left(\frac{1}{s} \partial_s (s \partial_s) + \frac{1}{s^2} \partial_{\phi\phi} + \partial_{zz} \right) W = n(s, \mathbf{y}) \qquad \text{for } s > r_1 \tag{12b}$$

with continuously differentiable W, i.e., with the interface conditions

$$W(r_1-,\mathbf{y}) = W(r_1+,\mathbf{y}),$$
$$\partial_s W(r_1-,\mathbf{y}) = \partial_s W(r_1+,\mathbf{y}).$$

We replace the original system (7) by its weak form by integrating it against a test function $\psi \in \mathcal{D}$ using the volume element $r\mathrm{d}r$ and integrating by parts. We find that

$$\begin{aligned}(13)\quad &-\epsilon_< \iint_{s<r_1} \left(W\frac{\mu^2}{r(s)}\partial_s(r(s)\partial_s\psi) + W\frac{1}{r(s)^2}\partial_{\phi\phi}\psi + W\partial_{zz}\psi \right)\frac{r(s)}{\mu}\mathrm{d}s\mathrm{d}\mathbf{y} \\ &-\epsilon_> \iint_{s>r_1} \left(W\frac{1}{s}\partial_s(s\partial_s\psi) + W\frac{1}{s^2}\partial_{\phi\phi}\psi + W\partial_{zz}\psi \right) s\mathrm{d}s\mathrm{d}\mathbf{y} \\ &= \iint n(r,\mathbf{y})\psi(r,\mathbf{y})r\mathrm{d}r\mathrm{d}\mathbf{y}\end{aligned}$$

holds for all ψ. We assume that ψ and its derivatives vanish identically at the boundaries of the simulation domain Ω so that no extra terms arise from the boundary conditions there. We now pass to the limit $\lambda \to 0$ in the weak formulation (13). First, we set

$$(14a)\qquad U^< := \iint_{r<r_1} n_<(r,\mathbf{y})\psi(r,\mathbf{y})r\mathrm{d}r\mathrm{d}\mathbf{y},$$

$$(14b)\qquad U^> := \iint_{r>r_1} \chi\left(r_1 + \frac{r-r_1}{\lambda}, \frac{1}{\lambda}\mathbf{y}, \mathbf{y}\right)\psi(r,\mathbf{y})r\mathrm{d}r\mathrm{d}\mathbf{y},$$

so that $\iint u(r,\mathbf{y})\psi(r,\mathbf{y})r\mathrm{d}r\mathrm{d}\mathbf{y} = U^< + U^>$. Now we have to determine the limit

$$U_0^> := \lim_{\lambda\to 0} U^>,$$

and then the limiting equation is given by

$$\begin{aligned}(15)\quad &-\epsilon_< \iint_{s<r_1} \left(W\frac{\mu^2}{r(s)}\partial_s(r(s)\partial_s\psi) + W\frac{1}{r(s)^2}\partial_{\phi\phi}\psi + W\partial_{zz}\psi \right)\frac{r(s)}{\mu}\mathrm{d}s\mathrm{d}\mathbf{y} \\ &-\epsilon_> \iint_{s>r_1} \left(W\frac{1}{s}\partial_s(s\partial_s\psi) + W\frac{1}{s^2}\partial_{\phi\phi}\psi + W\partial_{zz}\psi \right) s\mathrm{d}s\mathrm{d}\mathbf{y} \\ &= U^< + U_0^>.\end{aligned}$$

The limit of $\boldsymbol{U^>}$. To compute $U_0^>$, we write

$$U^> = \sum_{\substack{1\le m_1\le N_1\\ 1\le m_2\le N_2}} \int_{\mathcal{C}_\mathbf{m}} \int_{r_1}^{r_2} \chi\left(r_1 + \frac{r-r_1}{\lambda}, \frac{1}{\lambda}\mathbf{y}, \mathbf{y}\right)\psi(r,\mathbf{y})r\mathrm{d}r\mathrm{d}\mathbf{y}$$

and substitute

$$\rho := r_1 + \frac{r-r_1}{\lambda},$$
$$\mathbf{y} =: \lambda\mathbf{m} + \lambda\boldsymbol{\eta},$$

so that $\boldsymbol{\eta} \in L$, which yields

$$U^{>} = \lambda^3 \sum_{\substack{1\le m_1\le N_1\\ 1\le m_2\le N_2}} \int_L \int_{r_1}^{r_2} \psi(r_1+\lambda(\rho-r_1), \lambda\mathbf{m}+\lambda\boldsymbol{\eta})\chi(\rho,\boldsymbol{\eta},\lambda\mathbf{m}+\lambda\boldsymbol{\eta}) \cdot \big(r_1+\lambda(\rho-r_1)\big)\mathrm{d}\rho\mathrm{d}\boldsymbol{\eta}.$$

Let $\rho_{\max} \in \mathbb{R}^+$ be arbitrary and independent of λ. Since ψ is an arbitrary test function, we can choose ψ to be supported only in a $\rho_{\max}$-neighborhood of r_1; i.e., $\psi(r_1+\lambda(\rho-r_1), \lambda\mathbf{m}+\lambda\boldsymbol{\eta})$ vanishes for $|\rho-r_1| > \rho_{\max}$. Therefore we have $|\lambda(\rho-r_1)| \ll 1$ for the first argument of ψ and we have $\|\lambda\boldsymbol{\eta}\| \ll 1$ for the second argument, since $\boldsymbol{\eta} \in L$ is bounded. Hence the Taylor expansion of ψ in $\lambda(\rho-r_1)$ and $\lambda\boldsymbol{\eta}$ yields

$$\psi(r_1+\lambda(\rho-r_1), \lambda\mathbf{m}+\lambda\boldsymbol{\eta}) = \psi(r_1,\lambda\mathbf{m}) + \lambda(\rho-r_1)\partial_r\psi(r_1,\lambda\mathbf{m}) + \lambda\boldsymbol{\eta}\cdot\nabla_{\mathbf{y}}\psi(r_1,\lambda\mathbf{m}) + O(\lambda^2),$$

and the expansion of χ in $\lambda\boldsymbol{\eta}$ yields

$$\chi(\rho,\boldsymbol{\eta},\lambda\mathbf{m}+\lambda\boldsymbol{\eta}) = \chi(\rho,\boldsymbol{\eta},\lambda\mathbf{m}) + \lambda\boldsymbol{\eta}\cdot\nabla_{\mathbf{y}}\chi(\rho,\boldsymbol{\eta},\lambda\mathbf{m}) + O(\lambda^2).$$

Dropping terms of order $O(\lambda^2)$ and higher, we obtain

$$U^{>} = \lambda^3 \sum_{\substack{1\le m_1\le N_1\\ 1\le m_2\le N_2}} \int_L \int_{r_1}^{r_2} \big(\big(\psi(r_1,\lambda\mathbf{m}) + \lambda(\rho-r_1)\partial_r\psi(r_1,\lambda\mathbf{m}) + \lambda\boldsymbol{\eta}\cdot\nabla_{\mathbf{y}}\psi(r_1,\lambda\mathbf{m})\big)\chi(\rho,\boldsymbol{\eta},\lambda\mathbf{m}) + \psi(r_1,\lambda\mathbf{m})\lambda\boldsymbol{\eta}\cdot\nabla_{\mathbf{y}}\chi(\rho,\boldsymbol{\eta},\lambda\mathbf{m})\big)\big(r_1+\lambda(\rho-r_1)\big)\mathrm{d}\rho\mathrm{d}\boldsymbol{\eta},$$

which is the Riemann sum of

$$U^{>} = \frac{\lambda}{2\pi r_1 L_z}\int_L\int_L\int_{r_1}^{r_2} \big(\psi(r_1,\mathbf{y})\chi(\rho,\boldsymbol{\eta},\mathbf{y}) + \lambda(\rho-r_1)\partial_r\psi(r_1,\mathbf{y})\chi(\rho,\boldsymbol{\eta},\mathbf{y}) + \lambda\boldsymbol{\eta}\cdot\nabla_{\mathbf{y}}(\psi(r_1,\mathbf{y})\chi(\rho,\boldsymbol{\eta},\mathbf{y}))\big)\big(r_1+\lambda(\rho-r_1)\big)\mathrm{d}\rho\mathrm{d}\boldsymbol{\eta}r_1\mathrm{d}\mathbf{y}.$$

Using Definitions 2 and 3 and the divergence theorem finally yields

$$U_0^{>} = \int_L \big(\psi(r_1,\mathbf{y})C(\mathbf{y}) + \partial_r\psi(r_1,\mathbf{y})D_r(\mathbf{y})\big)r_1\mathrm{d}\mathbf{y}. \tag{16}$$

The strong formulation and the resulting interface conditions. Thus the weak formulation of the homogenized problem is given by the limiting equation (15), with the limiting term $U_0^{>}$ given by (16). We now formulate the problem in a strong sense; i.e., we find a pointwise solution of (12) that satisfies interface conditions on the solution and its derivative at $r = r_1$. So we compare the limiting equation (15) to the solution of the problem

$$-\epsilon_{<}\left(\frac{\mu^2}{r(s)}\partial_s(r(s)\partial_s) + \frac{1}{r(s)^2}\partial_{\phi\phi} + \partial_{zz}\right)W_h = n_{<}(r(s),\mathbf{y}) \quad \text{for } s < r_1, \tag{17a}$$

$$-\epsilon_{>}\left(\frac{1}{s}\partial_s(s\partial_s) + \frac{1}{s^2}\partial_{\phi\phi} + \partial_{zz}\right)W_h = 0 \quad \text{for } s > r_1. \tag{17b}$$

Summing (17a) and (17b), integrating by parts, and using the definition (14a) of $U^<$ yields

$$
\begin{aligned}
(18)\quad & -\epsilon_< \iint_{s<r_1} \left(W_h \frac{\mu^2}{r(s)} \partial_s (r(s) \partial_s \psi) + W_h \frac{1}{r(s)^2} \partial_{\phi\phi} \psi + W_h \partial_{zz} \psi \right) \frac{r(s)}{\mu} \mathrm{d}s\mathrm{d}\mathbf{y} \\
& -\epsilon_> \iint_{s>r_1} \left(W_h \frac{1}{s} \partial_s (s \partial_s \psi) + W_h \frac{1}{s^2} \partial_{\phi\phi} \psi + W_h \partial_{zz} \psi \right) s \mathrm{d}s\mathrm{d}\mathbf{y} \\
& + \int -\epsilon_< \mu r_1 \partial_s W_h(r_1-) \psi(r_1) + \epsilon_< \mu r_1 W_h(r_1-) \partial_s \psi(r_1) \\
& \qquad + \epsilon_> r_1 \partial_s W_h(r_1+) \psi(r_1) - \epsilon_> r_1 W_h(r_1+) \partial_s \psi(r_1) \mathrm{d}\mathbf{y} = U^<.
\end{aligned}
$$

Since W_h must satisfy the limiting equation (15) at the same time, we subtract the limiting equation (15) from (18), and using (16) for $U_0^>$ we obtain

$$
\begin{aligned}
\int & \big(-\epsilon_< \mu r_1 \partial_s W_h(r_1-) + \epsilon_> r_1 \partial_s W_h(r_1+) \big) \psi(r_1) \\
& + \big(\epsilon_< \mu r_1 W_h(r_1-) - \epsilon_> r_1 W_h(r_1+) \big) \partial_s \psi(r_1) \mathrm{d}\mathbf{y} \\
& = -U_0^> = -\int_L \big(C(\mathbf{y}) \psi(r_1, \mathbf{y}) + D_r(\mathbf{y}) \partial_s \psi(r_1, \mathbf{y}) \big) r_1 \mathrm{d}\mathbf{y}.
\end{aligned}
$$

This equation must hold for all test functions ψ. Therefore we compare the coefficients of $\psi(r_1)$ and $\partial_s \psi(r_1)$, which yields

$$
\begin{aligned}
\epsilon_> \partial_s W_h(r_1+) - \epsilon_< \mu \partial_s W_h(r_1-) &= -C(\mathbf{y}), \\
\epsilon_> W_h(r_1-) - \epsilon_> W_h(r_1+) &= -D_r(\mathbf{y}).
\end{aligned}
$$

To revert from the stretched variables, we use the definitions (10) and (11) of W and s to find the homogenized problem

$$
\begin{aligned}
-\epsilon_< \left(\frac{1}{r} \partial_r (r \partial_r) + \frac{1}{r^2} \partial_{\phi\phi} + \partial_{zz} \right) V_h(r, \mathbf{y}) &= n_< \quad \text{for } r < r_1, \\
-\epsilon_> \left(\frac{1}{r} \partial_r (r \partial_r) + \frac{1}{r^2} \partial_{\phi\phi} + \partial_{zz} \right) V_h(r, \mathbf{y}) &= 0 \qquad \text{for } r > r_1,
\end{aligned}
$$

together with the interface conditions

$$
\begin{aligned}
\epsilon_> \partial_r V_h(r_1+) - \epsilon_< \partial_r V_h(r_1-) &= -C(\mathbf{y}), \\
V_h(r_1+) - V_h(r_1-) &= \frac{D_r(\mathbf{y})}{\epsilon_>},
\end{aligned}
$$

as claimed in (8) and (9). This concludes the proof. □

The Poisson equation (8) with the interface conditions (9) shows that the multiscale problem of modeling the quasi-periodic layer of biomolecules attached to a surface is solved by replacing the atomic structure of the boundary layer and its partial charges by certain interface conditions.

We remark that the formal calculation of the theorem does not establish the convergence of the solutions of the original problem to the solution of the limiting problem for $\lambda \to 0$, but it states that if the solutions converge, the limit has to satisfy the limiting problem (8), (9).

The existence and uniqueness of the solution of the limiting problem (8), (9) can be shown as follows. By extending $D_r(\mathbf{y})/\epsilon_>$ to Ω and adding this extension on one side of the interface, the jump in (9a) is removed. In the weak formulation of (8), partial integration contributes the integral

$$\int \big(\epsilon_< \partial_r V_h(r_1-)\psi(r_1) - \epsilon_> \partial_r V_h(r_1+)\psi(r_1)\big) r_1 \mathrm{d}\mathbf{y} = \int C(\mathbf{y})\psi(r_1) r_1 \mathrm{d}\mathbf{y},$$

not depending on V_h due to (9b), to the right-hand side. Applying the Lax–Milgram theorem yields the existence and uniqueness of the solution in $H^1(\Omega)$ under the assumptions of Theorem 4 and $C \in L^2$, $D_r \in H^1$.

2.4. Planar structures. The interface conditions for planar structures can be derived from the conditions for cylindrical structures by taking the limit $r \to \infty$. Let (x, y, z) be the Cartesian coordinate system with the origin on the transducer-liquid interface at the source contact so that the positive x-axis points into the liquid and the negative x-axis into the transducer. The simulation domain is $\Omega := [x_1, x_2] \times [y_1, y_2] \times [z_1, z_2] \subset \mathbb{R}^3$ with $x_1 < 0 < x_2$ and the surface of the transducer is $L_1 \cdot L_2$ with $L_1 := y_2 - y_1$ and $L_2 := z_2 - z_1$. We also define $\mathbf{y} := (y, z)$ and the fast variables $\xi := \frac{1}{\lambda} x$ and $\boldsymbol{\eta} := \frac{1}{\lambda}\mathbf{y}$. Then the surface charge density C_{pl} and the dipole moment density D_{pl} with respect to x are given by

$$C_{\mathrm{pl}}(\mathbf{y}) := \frac{\lambda}{L_1 L_2} \int_L \int_{\mathbb{R}^+} \chi(\xi, \boldsymbol{\eta}, \mathbf{y}) \mathrm{d}\xi \mathrm{d}\boldsymbol{\eta},$$

$$D_{\mathrm{pl}}(\mathbf{y}) := \frac{\lambda^2}{L_1 L_2} \int_L \int_{\mathbb{R}^+} \xi \chi(\xi, \boldsymbol{\eta}, \mathbf{y}) \mathrm{d}\xi \mathrm{d}\boldsymbol{\eta}.$$

Taking the limit $r \to \infty$ in Theorem 4 yields this corollary.

COROLLARY 5. *Under the conditions of Theorem* 4*, the limiting problem for* $\lambda \to 0$ *of the boundary value problem*

$$\begin{aligned} -\nabla \cdot \big(\epsilon(x)\nabla\big) V(x, \mathbf{y}) &= n(x, \mathbf{y}), \\ V(0-, \mathbf{y}) &= V(0+, \mathbf{y}), \\ \epsilon_< \partial_x V(0-, \mathbf{y}) &= \epsilon_> \partial_x V(0+, \mathbf{y}) \end{aligned}$$

with $(x, \mathbf{y}) \in \Omega$ *is the boundary value problem*

$$\begin{aligned} -\epsilon_< \Delta V_h(x, \mathbf{y}) &= n_<(x, \mathbf{y}) \quad && \text{for } x < 0, \\ -\epsilon_> \Delta V_h(x, \mathbf{y}) &= 0 && \text{for } x > 0 \end{aligned}$$

with the interface conditions

$$\begin{aligned} V_h(0+, \mathbf{y}) - V_h(0-, \mathbf{y}) &= \frac{D_{\mathrm{pl}}(\mathbf{y})}{\epsilon_>}, \\ \epsilon_> \partial_x V_h(0+, \mathbf{y}) - \epsilon_< \partial_x V_h(0-, \mathbf{y}) &= -C_{\mathrm{pl}}(\mathbf{y}). \end{aligned}$$

3. Simulation results.

3.1. Numerical verification in one dimension. To verify the homogenization result numerically, we compare nonhomogenized and homogenized one-dimensional problems and their solutions. In the first problem, the charge distribution χ in the boundary layer is given by the sum of two delta distributions, and a very fine equidistant grid in the r-direction is used. In the second problem, the same grid is used, but now the interface conditions depending on $C(\chi)$ and $D_r(\chi)$ are implemented instead of the inclusion of χ. This setup is important for the application of this method to real-world problems as treated below and enables us to observe how well nonhomogenized and homogenized solutions agree.

We first show how two delta distributions can be used to construct a charge distribution with given arbitrary values c and d for the surface charge density and dipole moment density. If the interface is again at r_1 and the charge distribution is

$$\chi(r) = \alpha\delta(r - r_1) + \beta\delta(r - r_2) \tag{19}$$

with $r_1 < r_2$, then we have

$$C(\chi) := \frac{1}{r_1}\int_{r_1}^{\infty} \chi(r) r \mathrm{d}r = \alpha + \frac{r_2}{r_1}\beta,$$
$$D_r(\chi) := \frac{1}{r_1}\int_{r_1}^{\infty} (r - r_1)\chi(r) r \mathrm{d}r = \frac{(r_2 - r_1)r_2}{r_1}\beta$$

for the one-dimensional problem before taking the limit $\lambda \to 0$. There are two important cases. For given values $c \in \mathbb{R}$ and $d = 0$, we choose $\alpha := c$ and $\beta := 0$. For given values $c = 0$ and $d \in \mathbb{R}$, we set

$$\alpha := -\frac{d}{r_2 - r_1} \qquad \text{and} \qquad \beta := \frac{r_1 d}{(r_2 - r_1)r_2}. \tag{20}$$

Figure 2 shows numerical results for these two cases and two mixed cases. Excellent quantitative agreement is found.

3.2. Numerical verification in two dimensions. In the two-dimensional numerical verification, one axis (the r-axis) is perpendicular to the boundary layer, and the second direction (the z-axis) is parallel to the boundary layer. In the two-dimensional verification the effects of different boundary conditions on the solutions before and after homogenization are investigated as well. In all simulations we apply Dirichlet boundary conditions at the electrode in the liquid, i.e., $V(r = r_2) = 0$, and Neumann boundary conditions at the rest of the boundary in the liquid, i.e., $\partial_r V(r \geq r_1, z = 0) = 0$ and $\partial_r V(r \geq r_1, z = L_z) = 0$. The two cases of Neumann and Dirichlet boundary conditions in the figures refer to the contacts: in the first case, zero Neumann boundary conditions are used at the source and drain contacts, i.e., $\partial_r V(r < r_1, z = 0) = 0$ and $\partial_r V(r < r_1, z = L_z) = 0$, and in the second case zero Dirichlet boundary conditions are used there, i.e., $V(r < r_1, z = 0) = 0$ and $V(r < r_1, z = L_z) = 0$.

In the examples, there are ten boxes and each box extends 4 nm in the z-direction. Each box contains two delta distributions that are centered in the z-direction and have coefficients according to (20), i.e.,

$$\chi(r, z) := \sum_{i=1}^{10} \alpha_i \delta(r - 20\,\mathrm{nm})\delta(z - z_i) + \beta_i \delta(r - 21\,\mathrm{nm})\delta(z - z_i)$$

with $z_i = \{2, 6, 10, \ldots, 38\}$.

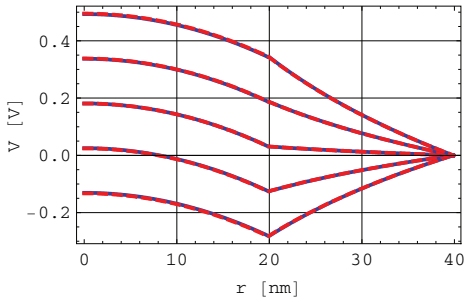

(a) C from $-0.1\,\mathrm{q}\cdot\mathrm{nm}^{-2}$ (bottom lines) to $0.1\,\mathrm{q}\cdot\mathrm{nm}^{-2}$ (top lines) and $D_r = 0$.

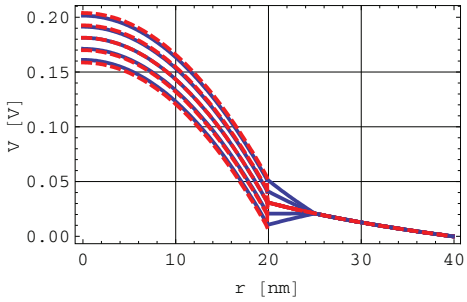

(b) $C = 0$ and D_r from $-0.1\,\mathrm{q}\cdot\mathrm{nm}^{-1}$ (bottom lines) to $0.1\,\mathrm{q}\cdot\mathrm{nm}^{-1}$ (top lines).

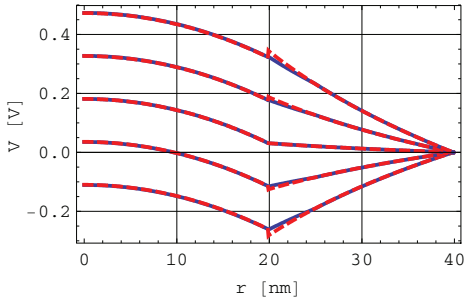

(c) $C = D_r/\mathrm{nm}$ from $-0.1\,\mathrm{q}\cdot\mathrm{nm}^{-2}$ (bottom lines) to $0.1\,\mathrm{q}\cdot\mathrm{nm}^{-2}$ (top lines).

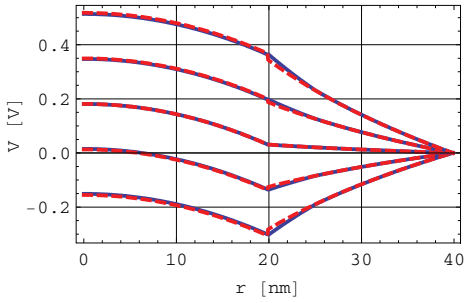

(d) $C = -D_r/\mathrm{nm}$ from $-0.1\,\mathrm{q}\cdot\mathrm{nm}^{-2}$ (bottom lines) to $0.1\,\mathrm{q}\cdot\mathrm{nm}^{-2}$ (top lines).

FIG. 2. *The electrostatic potential as function of radius. The grid spacing is* 0.125 nm, $r_1 = 20\,\mathrm{nm}$, $r_2 = 25\,\mathrm{nm}$, *and the silicon* ($r \le 20\,\mathrm{nm}$) *is p-doped with* $10^{18}\,\mathrm{q}\cdot\mathrm{cm}^{-3}$. *The solid lines are the solutions of equation* (1) *with the charge density* χ *given by* (19) *and* (20), *whereas the dashed lines are the solutions of the homogenized problem with the interface conditions. In* (a), *the surface charge density* C *is varied while the dipole moment density* D_r *vanishes; in* (b), C *vanishes while* D_r *varies; and in* (c) *and* (d) *both values vary simultaneously.*

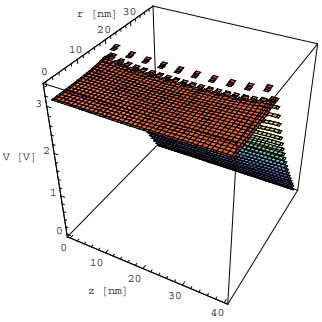

(a) Before homogenization.

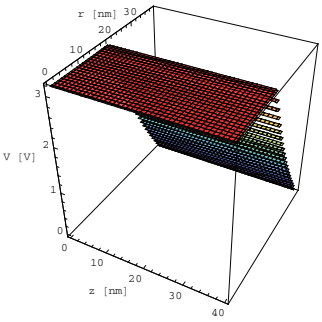

(b) After homogenization.

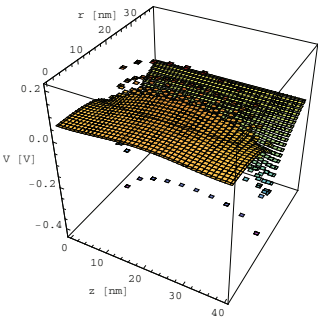

(c) Absolute error.

FIG. 3. *Numerical verification for* $C = 1\,\mathrm{q}\cdot\mathrm{nm}^{-2}$ *and* $D = 0$ *and Neumann boundary conditions.*

In Figures 3 to 8 the solution of the Poisson equation with charges given by χ, the solution of the homogenized problem with interface conditions, and the absolute error between these two solutions are shown for different combinations of the surface charge density C, of the dipole moment density D, and of Neumann or Dirichlet boundary

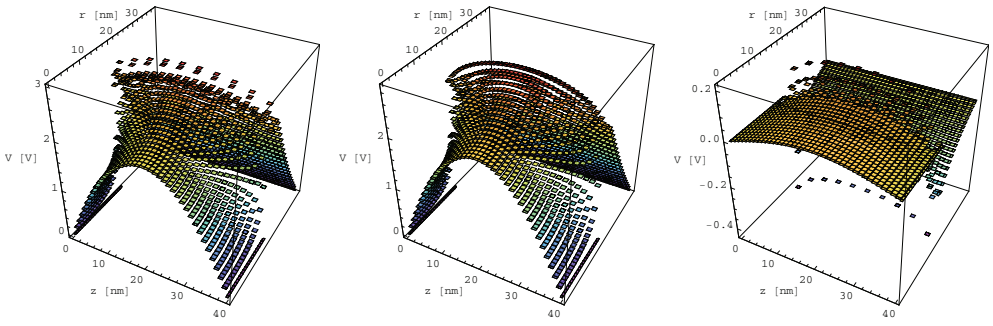

(a) Before homogenization. (b) After homogenization. (c) Absolute error.

FIG. 4. *Numerical verification for* $C = 1\,\mathrm{q}\cdot\mathrm{nm}^{-2}$ *and* $D = 0$ *and Dirichlet boundary conditions.*

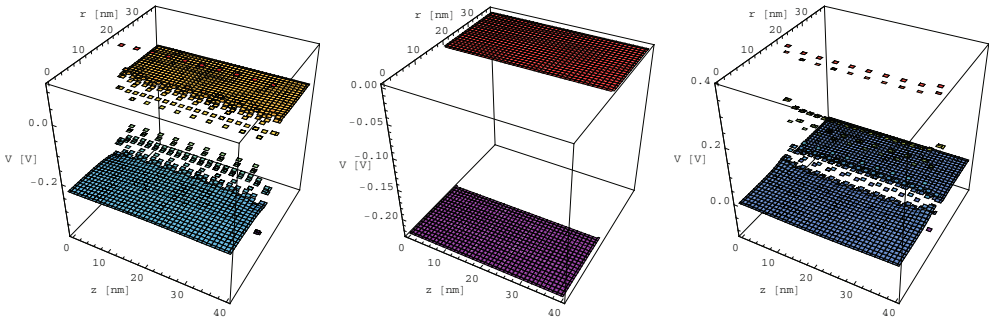

(a) Before homogenization. (b) After homogenization. (c) Absolute error.

FIG. 5. *Numerical verification for* $C = 0$ *and* $D = 1\,\mathrm{q}\cdot\mathrm{nm}^{-1}$ *and Neumann boundary conditions.*

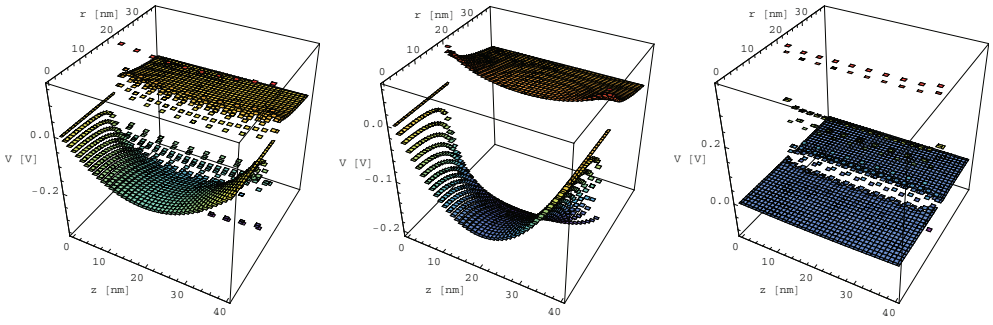

(a) Before homogenization. (b) After homogenization. (c) Absolute error.

FIG. 6. *Numerical verification for* $C = 0$ *and* $D = 1\,\mathrm{q}\cdot\mathrm{nm}^{-1}$ *and Dirichlet boundary conditions.*

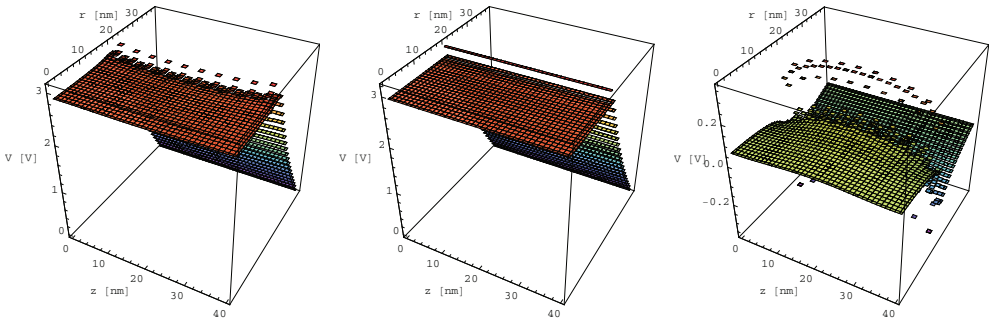

(a) Before homogenization. (b) After homogenization. (c) Absolute error.

FIG. 7. *Numerical verification for* $C = 1\,\mathrm{q}\cdot\mathrm{nm}^{-2}$ *and* $D = 1\,\mathrm{q}\cdot\mathrm{nm}^{-1}$ *and Neumann boundary conditions.*

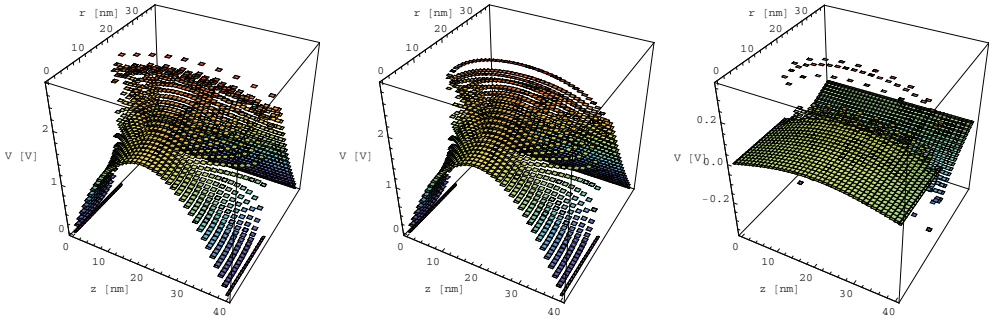

(a) Before homogenization. (b) After homogenization. (c) Absolute error.

FIG. 8. *Numerical verification for* $C = 1\,\mathrm{q}\cdot\mathrm{nm}^{-2}$ *and* $D = 1\,\mathrm{q}\cdot\mathrm{nm}^{-1}$ *and Dirichlet boundary conditions.*

conditions. In all cases the error does not exceed a few percent. This validates using the homogenized problem as a substitute for the original problem even for this small number of realistically sized boxes.

3.3. Results from the simulation of nanowire biosensors. The stationary drift-diffusion model for charge transport [1, 9] consists of five partial differential equations,

$$-\nabla\cdot\big(\epsilon\nabla V\big) = C + p - n, \tag{21a}$$

$$\nabla\cdot J_n = R, \tag{21b}$$

$$\nabla\cdot J_p = -R, \tag{21c}$$

$$J_n = D_n\nabla n - \mu_n n\nabla V, \tag{21d}$$

$$J_p = -D_p\nabla p - \mu_p p\nabla V. \tag{21e}$$

Here V denotes the electric potential, C is the concentration of fixed charges, i.e., the doping concentration, n and p are the concentrations of mobile charge carriers, i.e., electrons and holes, and J_n and J_p are the densities of the electron and hole currents. ϵ is the permittivity and D_n, D_p, μ_n, and μ_p are the diffusion coefficients and mobilities of electrons and holes. The first equation is the Poisson equation, the

second and third equations mean that charge sources are given by the recombination rate R, and the last two equations mean that the current densities are the sums of two terms: the first is proportional to the gradients of the charge concentrations (the diffusion part), and the second is proportional to the electric field $-\nabla V$ (the drift or advection part of the model).

In the case of biosensors, the simulation domain Ω includes the semiconductor, the dielectric layer, and the liquid as shown in Figure 1. The boundary $\partial\Omega$ of the domain Ω consists of a Dirichlet part $\partial\Omega_D$ and a Neumann part $\partial\Omega_N$ with $\partial\Omega_D \cap \partial\Omega_N = \emptyset$. Ohmic contacts at semiconductors give rise to Dirichlet boundary conditions where the potential V and the charge concentrations n and p are prescribed. At ohmic contacts at semiconductors the space charge vanishes, i.e., $C+p-n=0$ on $\partial\Omega_D$, and the system is in thermal equilibrium, i.e., $np = n_i^2$ on $\partial\Omega_D$, where n_i is the intrinsic charge density of the semiconductor material. Furthermore, the quasi-Fermi levels Φ_n and Φ_p are defined by

$$\Phi_n := V - U_T \ln\left(\frac{n}{n_i}\right),$$
$$\Phi_p := V + U_T \ln\left(\frac{p}{n_i}\right),$$

and assume the values of the applied voltage U at ohmic contacts, i.e., $\Phi_n = U = \Phi_p$. U_T is the thermal voltage and has a value of $\approx 0.025\,\mathrm{V}$ at room temperature. From these three conditions we find the Dirichlet boundary conditions

(22a)
$$n(x) = n_D(x) := \frac{1}{2}\left(C(x) + \sqrt{C(x)^2 + 4n_i^2}\right) \qquad \forall x \in \partial\Omega_D,$$

(22b)
$$p(x) = p_D(x) := \frac{1}{2}\left(-C(x) + \sqrt{C(x)^2 + 4n_i^2}\right) \qquad \forall x \in \partial\Omega_D,$$

(22c)
$$V(x) = V_D(x) := U(x) + U_T \ln\left(\frac{n_D(x)}{n_i}\right) = U(x) - U_T \ln\left(\frac{p_D(x)}{n_i}\right) \qquad \forall x \in \partial\Omega_D.$$

The Neumann parts $\partial\Omega_N$ of the boundary are insulating or artificial surfaces, and hence the currents and the electric field vanish in the normal direction to the surface. This yields the three Neumann boundary conditions

(23a) $$\nabla V(x) \cdot \mathbf{n} = 0 \qquad \forall x \in \partial\Omega_N,$$

(23b) $$J_n(x) \cdot \mathbf{n} = 0 \qquad \forall x \in \partial\Omega_N,$$

(23c) $$J_p(x) \cdot \mathbf{n} = 0 \qquad \forall x \in \partial\Omega_N.$$

In summary, the stationary drift-diffusion problem is given by the equations (21) with the boundary conditions (22) and (23). For the simulation of biosensors, the biofunctionalized surface layer is replaced by the interface conditions (9) at the transducer-liquid interface (i.e., at $r = r_1$ in Figure 1).

The most common model for the recombination rate R is the Shockley–Read–Hall term

$$R_{SRH} := \frac{np - n_i^2}{\tau_p(n + n_i) + \tau_n(p + n_i)},$$

TABLE 1
The variables and their units in a scaling suitable for numerical work.

Meaning	Variable	Unit or value
Length	r, z, L, ρ	nm
Angle	ϕ	1
Spatial ratio	λ	1
Time		ps
Temperature	T	K
Electric conversion factor	$1/(4\pi\epsilon_0)$	$138.935\,485\,\mathrm{kJ}\cdot\mathrm{mol}^{-1}\cdot\mathrm{nm}\cdot\mathrm{q}^{-2}$
Elementary charge	q	$\mathrm{q} = 1.602\,18\cdot 10^{-19}\mathrm{C}$
Boltzmann constant, gas constant	k	$8.314\,51\cdot 10^{-3}\mathrm{kJ}\cdot\mathrm{mol}^{-1}\cdot\mathrm{K}^{-1}$
Energy		$\mathrm{kJ}\cdot\mathrm{mol}^{-1}$
Electric potential	V, W, U, Φ	$\mathrm{kJ}\cdot\mathrm{mol}^{-1}\cdot\mathrm{q}^{-1} = 0.010\,364\,272\,\mathrm{V}$
Charge density	n, p, χ	$\mathrm{q}\cdot\mathrm{nm}^{-3}$
Macroscopic surface charge density	C	$\mathrm{q}\cdot\mathrm{nm}^{-2}$
Macroscopic dipole moment density	D_r	$\mathrm{q}\cdot\mathrm{nm}^{-1}$
Electron lifetime	τ_n	10^6 ps (silicon)
Hole lifetime	τ_p	10^7 ps (silicon)
Electron low-field mobility	μ_n	$1.5\cdot 10^5\,\mathrm{nm}^2\cdot\mathrm{V}^{-1}\cdot\mathrm{ps}^{-1}$ (silicon)
Hole low-field mobility	μ_p	$4.5\cdot 10^4\,\mathrm{nm}^2\cdot\mathrm{V}^{-1}\cdot\mathrm{ps}^{-1}$ (silicon)
Diffusion coefficient	D	$\mathrm{nm}^2\cdot\mathrm{ps}^{-1}$
Current flow	J	$\mathrm{q}\cdot\mathrm{nm}^2\cdot\mathrm{ps}^{-1}$
Recombination rate	R	$\mathrm{q}\cdot\mathrm{nm}^3\cdot\mathrm{ps}^{-1}$
Electric conductance	γ	S

where τ_n and τ_p are the lifetimes of electrons and holes. For the diffusion coefficients D_n and D_p we assume the Einstein relations

$$D_n = U_T\mu_n,$$
$$D_p = U_T\mu_p.$$

The variables and their units are summarized in Table 1.

To elucidate the physics of nanowire BioFETs, we apply the multiscale model and the drift-diffusion equations to the numerical simulation of silicon-nanowire BioFETs. The variables of the Poisson equation for the liquid and of the drift-diffusion model for the semiconductor are listed in Table 1. The electric potential of the electrode in the liquid and of the bulk liquid is assumed to be zero. This assumption is valid for small voltages applied to the electrode, since then the ions of the electrolyte screen the potential of the electrode and the bulk liquid is neutral. The charges in the boundary layer, i.e., the electric double layer and the biomolecules and their counter-ions, are included via the values of C and D_r. Since in experiments the conductance (or resistance) is recorded and published, we calculate the conductance of the nanowires.

The homogenization of the boundary layer has shown that the electric potential near the transducer-liquid boundary and therefore in the transducer depends on a higher order parameter, namely, the dipole moment density D_r of the biofunctionalized layer in addition to its surface charge density C. Hence the main question is how different values of C and D_r affect the conductance values and thus if the conductance measurements can be attributed to the field effect of target molecules. It can be argued that the charge density C of the cells in the biofunctionalized layer must (nearly) vanish because of the presence of counter-ions around the biomolecules and a reconfiguration of the electric double layer. Therefore the dipole moment of the boundary layer can provide the actual detection mechanism. In the following we therefore quantify the influence of the values of C and D_r on the conductance.

In one set of experiments [4], silicon nanowires with diameters from 5 nm to

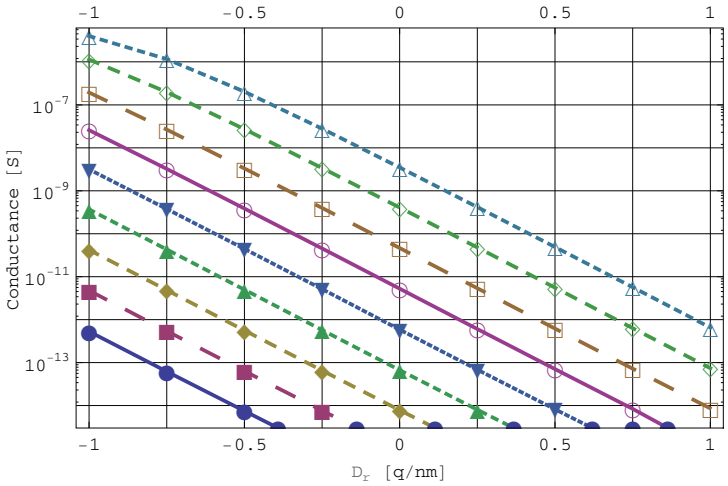

FIG. 9. *The conductance of a nanowire as a function of the dipole moment D_r for different values of the surface charge density C on a logarithmic scale. The bottom line (solid line with solid circles) is for $C = -0.1\,\mathrm{q}\cdot\mathrm{nm}^{-2}$; the top line (dashed line with hollow triangles) is for $C = +0.1\,\mathrm{q}\cdot\mathrm{nm}^{-2}$; the lines in between correspond to steps of $0.025\,\mathrm{q}\cdot\mathrm{nm}^{-2}$. The nanowire is p-doped with $10^{16}\mathrm{q}\cdot\mathrm{cm}^{-3}$, it is 50 nm long, the silicon core has a radius of 5 nm, and the silicon-oxide layer has a thickness of 2 nm.*

50 nm and lengths from 1 μm to 1000 μm were fabricated and the relative resistance change after binding of target ssDNA strands was recorded. A maximum resistance increase of 250% was measured. Unfortunately many important sensor parameters, especially those pertaining to the biofunctionalized layer, have not been characterized in the recently published BioFET experiments. This is certainly due to the fact that proper characterizations of, e.g., the nanowires, the probe spacing, the electric double layer, the counter-ions, and the orientations of the probe and target molecules involve separate research projects each.

Figure 9 shows the conductance of a nanowire sensor as a function of the surface charge density C and the dipole moment density D_r of the biofunctionalized surface layer. The figure shows that both C and D_r have an exponential influence on the conductance. Therefore not only the total charge of the boundary layer modulates the conductance of the transducer, but its dipole moment modulates the conductance as well.

This numerical evidence shows that the conductance variations in nanowire BioFETs upon binding of target molecules observed in experiments can be explained by a field effect. It also implies that higher order effects, i.e., the influence of the dipole moment of the biofunctionalized boundary layer, must be included in models and simulations of field-effect biosensors.

4. Conclusion. Recent experimental advances in the fabrication of nanowire BioFETs have not been matched by theoretical studies of their functioning. Qualitatively, their functioning is believed by experimentalists to be due to the field effect of the detected biomolecules on the semiconductor transducer [4, 15]. Regarding quantitative simulation, this work solves the underlying multiscale problem that arises from the different length scales of the biomolecules and the sensor surface areas, and hence provides the foundation for the self-consistent modeling of all the charges in the system, namely, in the semiconductor, in the biofunctionalized layer, and in the liquid.

Here the multiscale problem was solved by replacing the original Poisson equation and the fast-varying charge distribution in the biofunctionalized surface layer by an equivalent problem with interface conditions instead of the fast-varying charge distribution. The interface conditions take the effects of the charge and dipole moment of the biofunctionalized layer, including the biomolecules at the liquid-transducer interface, into account. In classical semiconductor device simulation, the boundary conditions at the gate contact that modulate conductance are Dirichlet boundary conditions. Here, in sensor simulation, the modeling is more involved. The electrode in the liquid is represented by Dirichlet boundary conditions as well, but the boundary layer at the liquid-transducer interface results in interface conditions. The boundary layer cannot be modeled just by its total charge; its dipole moment must be considered as well.

Using this multiscale model in combination with the drift-diffusion charge transport model, conductance simulations of realistically sized nanowire sensors were performed. The influence of the charge and especially of the dipole moment of the boundary layer was investigated numerically, and it was found that the dipole moment affects the conductance exponentially. It was concluded that simpler models including only the total charge are not sufficient. In fact, the change in dipole moment after binding of target molecules can be the primary detection mechanism.

The simulations results are in good quantitative agreement with published experiments. Measurements of the change in the resistance of a similar nanowire sensor show that it can be as large as 300% [4], and this large change can be explained by the numerical results in Figure 9. Unfortunately, a strict comparison with published measurements is difficult, because only a few measurements of a few different nanowire sensors fabricated by different groups are available. Parameters of the sensors such as density and orientation of immobilized molecules have not been determined, and complete electric characterizations of the devices have not been performed. This shows the importance of simultaneous simulation and characterization in elucidating the physics of BioFETs.

The simulation results show that different orientations of the biomolecules with respect to the surface, i.e., different dipole moments, affect the conductance of the transducer significantly. This implies that the investigation of the orientations of biomolecules at charged surfaces requires attention. Depending on the electric free-energy of the configuration, Brownian motion of the biomolecules may have great impact on the noise level of the biosensors and thus their sensitivity. This question is especially important for nanoscale sensors working at the detection limit.

Acknowledgments. The authors thank Dieter Baurecht, Alena Bulyha, Heidrun Karlic, Christoph Überhuber, and Franz Varga for discussions. The first author thanks Gordana Stojanovic for hospitality.

REFERENCES

[1] A. M. Anile, W. Allegretto, and C. Ringhofer, *Mathematical Problems in Semiconductor Physics*, Springer-Verlag, Berlin, 2003.

[2] A. Bulyha, C. Heitzinger, and N. Mauser, *Three-dimensional Monte Carlo simulation of biofunctionalized surface layers in the constant-voltage ensemble*, SIAM J. Sci. Comput., submitted.

[3] S. Damodaran, S. Vadivelmurugan, Q.-T. Do, C. Heitzinger, Y. Liu, R. Dutton, and G. Klimeck, *Investigation of the conductance of silicon nanowire biosensors using the* $2D$ *drift-diffusion model*, in Proceedings of the 10th NSTI Nanotech Conference 2007 (NSTI Nanotech 2007), Santa Clara, CA, 2007, pp. 1374/1–3.

[4] Z. Gao, A. Agarwal, A. D. Trigg, N. Singh, C. Fang, C.-H. Tung, Y. Fan, K. D. Buddharaju, and J. Kong, *Silicon nanowire arrays for label-free detection of DNA*, Analyt. Chem. A, 79 (2007), pp. 3291–3297.

[5] C. Heitzinger and G. Klimeck, *Investigation of conventional DNAFETs for genome-wide detection of polymorphisms*, in Proceedings of Eurosensors XX 2006, Vol. 1, Göteborg, Sweden, 2006, pp. 448–449.

[6] C. Heitzinger and G. Klimeck, *Computational aspects of the three-dimensional feature-scale simulation of silicon-nanowire field-effect sensors for DNA detection*, J. Comput. Electron., 6 (2007), pp. 387–390.

[7] C. Heitzinger, C. Ringhofer, and S. Selberherr, *Investigations of the potential jump at the surface of BioFETs using a multi-scale model*, in Proceedings of the 211th Meeting of the Electrochemical Society (ECS), Chicago, IL, 2007, The Electrochemical Society, Pennington, NJ, 2007, p. 947.

[8] J. F. Klemic, E. Stern, and M. A. Reed, *Hotwiring biosensors*, Nature Biotechnol., 19 (2001), pp. 924–925.

[9] P. A. Markowich, C. A. Ringhofer, and C. Schmeiser, *Semiconductor Equations*, Springer-Verlag, Wien, 1990.

[10] F. Patolsky, G. Zheng, and C. M. Lieber, *Fabrication of silicon nanowire devices for ultrasensitive, label-free, real-time detection of biological and chemical species*, Nature Protocols, 1 (2006), pp. 1711–1724.

[11] A. W. Peterson, R. J. Heaton, and R. M. Georgiadis, *The effect of surface probe density on DNA hybridization*, Nucleic Acids Res., 29 (2001), pp. 5163–5168.

[12] A. Poghossian, A. Cherstvy, S. Ingebrandt, A. Offenhäuser, and M. J. Schöning, *Possibilities and limitations of label-free detection of DNA hybridization with field-effect-based devices*, Sensors and Actuators B, 111-112 (2005), pp. 470–480.

[13] M. J. Schöning and A. Poghossian, *Recent advances in biologically sensitive field-effect transistors (BioFETs)*, Analyst, 127 (2002), pp. 1137–1151.

[14] M. J. Schöning and A. Poghossian, *Bio FEDs (field-effect devices): State-of-the-art and new directions*, Electroanalysis, 18 (2006), pp. 1893–1900.

[15] E. Stern, J. Klemic, D. Routenberg, P. Wyrembak, D. Turner-Evans, A. Hamilton, D. LaVan, T. Fahmy, and M. Reed, *Label-free immunodetection with CMOS-compatible semiconducting nanowires*, Nature, 445 (2007), pp. 519–522.

[16] G. Zheng, F. Patolsky, Y. Cui, W. U. Wang, and C. M. Lieber, *Multiplexed electrical detection of cancer markers with nanowire sensor arrays*, Nature Biotechnol., 23 (2005), pp. 1294–1301.